High-Speed Imaging to Quantify Transient Ice Accretion Process over an Airfoil

Rye M. Waldman[*] and Hui Hu[†]

Iowa State University, Ames, Iowa 50011

Ice accretion on aircraft wings poses a performance and safety threat as aircraft encounter supercooled droplets suspended in the cloud layer. The details of the ice accretion depend on the atmospheric conditions and the flight parameters. The icing process on the wing consists of a complex interaction of water deposition, surface water transport, and freezing. The aerodynamics affect the water deposition, the heat and mass transport, and ice accumulation; meanwhile, the accumulating ice affects the aerodynamics. Until now, most experimental measurements of aircraft icing have focused on the final ice shapes formed after exposure for a set duration to icing conditions. This approach fails to capture the transient processes that form the final ice formations. Here, we present experiments conducted in the Iowa State Icing Research Tunnel on a NACA 0012 airfoil to study the transient ice accretion process under varying icing conditions. High-speed video of the icing process was acquired under controlled environmental conditions to quantitatively measure the transient water film runback, rivulet formation, and accumulated ice growth. Image processing techniques were developed to extract physical information from the acquired image sequences of the icing events. The experiments demonstrate how varying the environmental conditions modifies the ice accretion process. It was found that the leading-edge ice growth rate is proportional to water deposition rate and the rivulet spacing and rivulet area coverage decrease with increasing wind speed. The water rivulet runback speed over the airfoil surface was found to increase rapidly with increasing wind speed.

Nomenclature

A	=	cross-sectional area
$\mathcal{A}$	=	rivulet image
A	=	image activity
AF	=	area fraction
a	=	ice accumulation parameter
c	=	chord length
D	=	diameter
I^i	=	ith image in the high-speed image sequence
I^i_{ref}	=	difference of the ith image with the reference image
i	=	image index
K	=	droplet inertia parameter (Stokes number)
L	=	characteristic length scale
LWC	=	liquid water content (mass of water per volume of air)
N	=	number of rivulets
T	=	temperature
t	=	time
U	=	freestream velocity
u_{film}	=	water film runback speed
u_{riv}	=	rivulet runback speed
V	=	volume
$\dot{V}$	=	volume flow rate
We	=	Weber number
w	=	rivulet width
x	=	coordinate axis aligned with chord
y	=	coordinate axis aligned with span
α	=	angle of attack
ΔI^i	=	difference of the ith image with the $(i-1)$th image, the image derivative
δ	=	rivulet spacing
μ	=	dynamic viscosity
ρ	=	density
σ	=	surface tension
τ	=	time duration

I. Introduction

ICE accretion poses a threat to the safety and performance of aircraft in cold weather, especially as the aircraft travels through the cloud layer and encounters supercooled liquid water droplets. The ice formation depends on the flight conditions and environmental parameters [1], and much effort has been spent to predict icing conditions using theoretical and computational models [2–5]. The Iowa State Icing Research Tunnel has been constructed to provide experimental data of aircraft icing conditions to inform the development of advanced icing models.

The ice forms a variety of structures as it forms on wings, and the details of the ice formation will vary with the environmental and operating conditions [6]. When operating conditions are cold and the air has a small liquid water content (LWC), the water droplets freeze immediately upon impact with the wing, forming rime ice. At warmer air temperatures, just below freezing and with larger LWC, the water accumulating on the wing does not immediately freeze, and mass transport along the surface of the wing can play an important role in the glaze ice formations and accretion.

During glaze ice formation, the deposited water droplets form a film of water and may generate rivulets that run back along the chord [3]. Instability of the accreting ice leads to the formation of surface roughness [7]. The surface roughness elements can enhance the local heat transfer [8] and disrupt the wing's aerodynamic performance [9]. The ice roughness elements that protrude out into the flow will capture impinging droplets faster and experience enhanced heat transfer compared to surrounding ice regions; therefore, protruding ice elements will grow faster than surrounding regions, amplifying ice roughness [10].

Detection of ice is an important process for monitoring the state of aircraft instruments and wings, and various techniques have been employed to detect the formation of ice [11]. Most of these techniques use single-point techniques that are capable at providing a time history of ice accretion information at a single point for each

sensor location. Embedding multipoint sensing systems with a scaled model on the order of 1 cm thick may be impractical for quantifying the distribution of icing over a wing surface. For the vast majority of ice accretion studies, measuring accreted ice shapes has been accomplished by cutting or melting into a final ice shape, and then tracing an outline of the accretion on a piece of paper or cardboard [12–18], which is both intrusive and provides measurement of the ice shape at only a single time. Photography has been used to measure accreted ice shapes in several studies (e.g., [15,16,19]). Shin and Bond [12] acquired images of ice accretions from a perpendicular angle and manually clicked image points to measure ice thickness. Vargas and Reshotko [16] and later Vargas and Tsao [15] each used macrophotography images of the ice shapes with a tape measure to characterize the ice accretion shapes. More recently, Kraj and Bibeau [19] used image analysis software to digitize snapshots acquired perpendicularly to the ice accretion to measure the accreted leading-edge ice thickness growth rate during active de-icing. With the exception of Kraj and Bibeau [19], all these of previous experiments have examined the accreted ice shapes and aerodynamic characteristics of a final shape at a specified time after the initial onset of icing; however, this approach ignores the importance of the transient water runback process that can redistribute the impinging water on the wing before it freezes [20]. The distribution of ice formations on the wing depends on the initial distribution of water; therefore, understanding the development of the ice accretion requires understanding the initial transient processes. Novel measurement techniques capable of providing time-resolved measurements are highly desirable to quantify the spatial distribution of water and ice throughout the accretion process.

In this study, a series of icing wind-tunnel experiments were conducted to capture high-speed videography of the ice accretion process on a NACA 0012 wing. Keeping the temperature, angle of attack, and liquid water content the same but varying the freestream air velocity leads to differences in the ice accretion process. The recorded images are digitized to extract quantitative measurements of transient icing features during the icing process.

II. Experimental Methods

All experiments were performed in the Iowa State University Icing Research Tunnel. The wind tunnel is a closed-loop type with a 25.4×25.4 cm^2 test section. The tunnel is refrigerated via a heat exchanger installed after the wind-tunnel fan. The heat exchanger is chilled by a 40 hp compressor (Vilter), and the operating temperature is set by a temperature controller that toggles the compressor on/off when the working temperature is above/below the set point. The wind tunnel can be cooled to $-20\,°C$. A K-type thermocouple and thermocouple controller (Omega, HH501BJK) monitored air temperature in the test section before and after each test; however, ice buildup on the temperature probe during the experiments precluded reliable in situ measurements. Icing conditions in the wind tunnel are generated by spraying finely atomized water droplets into the chilled air upstream of the test section. A diagram of the wind tunnel is given in Fig. 1.

The spray system consists of an array of three pneumatic atomizing spray nozzles (Spraying Systems Co., 1/8NPT-SU11) and pressure regulators to control the water line and airline pressures. The volume flow rate of water was monitored with a digital flow meter (Omega, FLR-1605A). Adjusting the pressure regulators on the air and water lines adjusted the mass flow rate of water; therefore, the liquid water content LWC = (mass of water)/(volume of air) could be set for each wind speed tested via pressure adjustments. Droplet size is controlled by the relative air and water pressures. The relationship between the liquid water content LWC, the wind speed U, and the volume flow rate of water $\dot{V}$ [Eq. (1)] assumes that all of the sprayed water is evenly distributed over the test section area A:

$$\text{LWC} = \frac{m_{\text{water}}}{V_{\text{air}}}, \quad = \frac{\rho \dot{V}}{A \cdot U} \quad (1)$$

The water density ρ relates the volume flow rate of water measured by the flow meter to the mass flow rate of water required by Eq. (1).
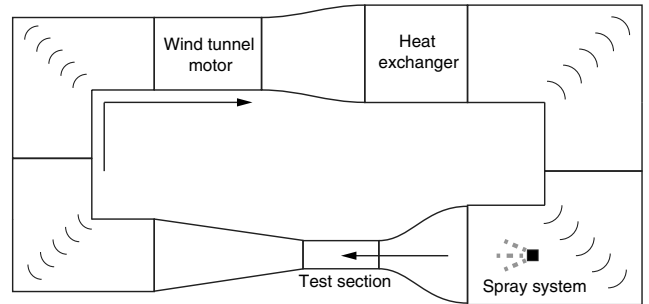

Fig. 1   Diagram of ISU icing research tunnel.

For each experiment, the volume flow rate of water was adjusted to achieve the desired liquid water content. The requisite volume flow rate was obtained by rearranging Eq. (1) for $\dot{V}$ as a function of the experiment conditions: $\dot{V} = \text{LWC} \cdot A \cdot U/\rho$. In all trials, the air pressure was set at least 10 psi higher than the water pressure to ensure that the generated droplets had a small mean volume diameter (15–100 μm). It should be noted that some fraction of the water sprayed into the wind tunnel could collect on the tunnel walls in the contraction section, and some of the droplets that pass above or below the wing may recirculate through the wind tunnel a second time. In the former case, deposition of water onto the wind-tunnel walls will tend to decrease the actual experiment LWC, whereas in the latter case, recirculation of the water droplets will tend to increase the LWC.

The experiments were conducted using a three-dimensionally printed NACA 0012 profile test wing that spanned the width of the test section. The wing chord length $c = 101.6$ mm. Supported by a stainless steel rod, the wing was mounted at its quarter-chord and oriented horizontally across the middle of the test section. The angle of attack was adjusted by pivoting the wing about the rod and fixing it at the desired angle measured with a digital inclinometer. The wing was finished with a coating of primer and wet-sanded to a smooth finish using 1000 grit sand paper.

High-speed video was recorded using a complementary metal-oxide semiconductor camera mounted 0.5 m above the wing (PCO Tech, Dimax) using a 60 mm macrolens (Nikon, 60 mm Nikkor 2.8D). The camera was positioned normal to the wing chord, providing a topdown view with a 1500×480 pixels^2 field of view and a pixel resolution of 11.74 pixels/mm. The camera was calibrated by placing a calibration target consisting of a grid of dots aligned in the plane defined by the wingspan and wing chord and computing a planar homography using the direct linear transform method, thus mapping the pixel coordinates to real-space coordinates projected onto the wing plane. The captured images were dewarped using this homography before extracting physical features.

Low-flicker illumination was provided by a pair of 150 W fiber-coupled halogen lamps (AmScope, HL250-AS). The experimental configuration is illustrated in Fig. 2. Each trial consisted of 8828 images acquired at a frame rate of 30 or 300 frames per second. The frame rate for each trial was chosen based on the freestream velocity, with the lowest freestream speeds (20 and 40 m/s) acquired at 30 frames per second and the highest freestream speed (60 m/s) acquired at 300 frames per second.

The experimental trials presented here were conducted at an air temperature of $T = -8°C$ and freestream velocities $U = 20, 40$, and 60 m/s, and the liquid water content for each speed tested was LWC = 1.1 g/m^3. The suction or pressure side of the test airfoil can be measured by setting a positive or negative angle of attack, respectively. The angle of attack was set at $\alpha = -5$ deg to observe the icing process on the pressure side of the wing, where the water film runback and rivulet formation is most prominent.

III. Description of the Icing Process

Icing occurs when supercooled water droplets suspended in the air are carried by the freestream and impact upon the body. The collection efficiency β specifies the distribution of water droplets
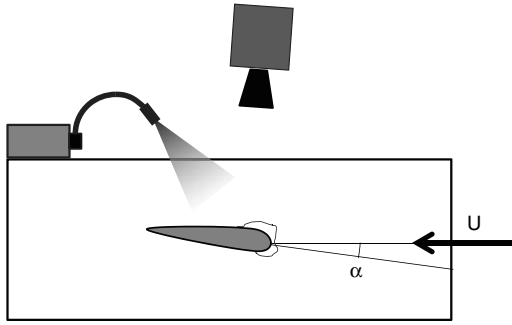
Fig. 2 Schematic of the test airfoil model and high-speed video imaging system.

impacting the body and is largely determined by the relative size of the droplets compared to the body and inertia. Heavy droplets follow ballistic trajectories to impinge on the body, whereas the smaller, lighter droplets are more inclined to follow streamlines and may miss the body altogether. The droplet trajectories, and consequently the collection efficiency, is determined by the droplet inertia parameter [14]:

$$K = \frac{\rho_w D^2 U}{18 L \mu} \qquad (2)$$

where ρ_w is the density of water, D is the droplet diameter, μ is the air viscosity, and L is a characteristic length of the body. For airfoils, this length L may be taken as the radius of curvature of the leading edge. Once deposited onto the body, the water may then be driven by aerodynamic shear stress in a Couette flow before freezing [2]. This aerodynamic driving force redistributes the water from where it was deposited to other regions of the body. Furthermore, the water film may break up into rivulets [21] as it runs back, creating a three-dimensional surface topology and affecting water collection and redistribution over the surface. The rivulet formation is governed by the interplay of surface tension forces and inertial forces; thus, the Weber number is an important parameter for determining the ice formation [14]:

$$We = \frac{\rho U^2 L}{\sigma} \qquad (3)$$

where ρ is the air density, and σ represents the water surface tension. The ice accretes according to a mass balance of water phases deposited on the wing, freezing into ice, and running back, and according to a heat balance of the water releasing latent heat during phase transition and the cooling action of convection and conduction [5]. Overall, the amount of ice that accretes relative to the size of the body is given by the accumulation parameter a [14]:

$$a = \frac{\text{LWC} \cdot U \cdot \tau}{L} \qquad (4)$$

Here, τ is the duration of water and ice accumulation. Equation (4) relates the ice accumulation to the rate that airborne water is carried toward the body with characteristic size L.

In the present study, a typical ice accretion trial at $U = 40$ m/s is examined first, and then the effect on the icing process as the freestream velocity changes is examined. The ice accretion process on the pressure side of a NACA 0012 wing with chord $c = 101.6$ mm, angle of attack $\alpha = 5$ deg, freestream velocity $U = 40$ m/s, liquid water content LWC $= 1.1$ g/m^3, and temperature $T = -8\,°C$ is given in Fig. 3. The ice accretion exhibits characteristics in agreement with previous works on icing [9]. First, the impinging water forms a film at the leading edge (Fig. 3a). As the film flows back along the wing, rivulets develop with fairly regular spacing (Fig. 3b). Near the leading edge, the water film begins to exhibit roughness due to instability [7,22], and water that was deposited ahead of the advancing water film can now be seen as nucleation points for feather growth in Figs. 3c and

3d. As the roughness elements grow and the ice layer thickens, the extent of the liquid water film begins to retreat back toward the leading edge (Fig. 3e). The roughness elements in the ice form wake regions, whereby flow separation forms behind the thickening ice sheet and prevents water from impinging behind the ice sheet. Only the ice feathers that reach out into the outer flow continue to grow outward and into the oncoming outer flow (Figs. 3f and 3g). When sufficient water accumulates in the ice roughness, aerodynamic forces splash water and deposit it on the wing behind the accumulated ice (the splash region is highlighted in the false-color inset and denoted by arrows in Fig. 3h).

At slower freestream velocities, i.e., for the test case of $U = 20$ m/s as shown in Fig. 4, the water film fails to break up into rivulets. In this case, the water impinges on the wing at the leading edge forms a film at the leading edge (Fig. 4a). A water film front forms (Fig. 4b), and water begins to bead up at the advancing film front; however, rivulets never develop by the time the water beads begin to solidify (Figs. 4c and 4d). Near the leading edge, the water film begins to exhibit roughness due to instability, and the water beads continue to accumulate water and grow Figs. 4e and 4f. Again, as the roughness elements grow and the ice layer thickens, the extent of the liquid water film begins to retreat back toward the leading edge (Fig. 4g), and the roughness elements in the ice form wake regions, whereby flow separation forms behind the thickening ice sheet and prevents water from impinging behind the ice sheet (Fig. 4h).

As the wind speed is increased to $U = 60$ m/s, the mass flow rate of water impinging on the wing increases, and the wind shear driving the water film flow increases in accordance with Eq. (4). The water film very quickly breaks into rivulets, which advance down the wing (Figs. 5b–5d) and have a smaller width and spacing than the slower freestream cases. Here, the rivulets exhibit narrower spacing between neighboring rivulets, and the rivulets advance farther downstream. The downstream extent of the water film begins to freeze (Fig. 5e). Near the leading edge, the water film begins to exhibit roughness (Fig. 5f). As the roughness elements grow and the ice layer thickens, the extent of the liquid water film begins to retreat back toward the leading edge (Figs. 5g and 5h).

Here, high-speed video of the ice accretion provides a qualitative view of the transient processes involved during icing, which lends some insight into the physics of ice formation. However, quantitative measurements of the ice features as they develop and evolve are needed to study the icing process in detail. Some methods are presented in the following section to extract measurements of the ice features from the high-speed video of the icing process.

IV. Digitizing Features in Icing Video

Extracting features from the raw video frames is not a straightforward process because there is no direct meaningful relationship between the pixel counts in the recorded image and the physical configuration of the water and ice (e.g., there is no direct relationship between the pixel count and the water depth, nor phase, etc.). The images are maps of the light intensity scattered or reflected from the wing, water, and ice. Light diffusely scattered from the wing or ice appears as grayscale values. Pixels that are saturated come from places with surface normals that direct specular reflections toward the camera.

Based on images such as those shown in Figs. 3–5, the human visual system can perform image processing and combine a priori knowledge to interpret the images as evolving ice shapes. Watching a video of the icing process provides the visual system with more information and context than viewing a single random snapshot of the process. By having information such as the initial image of the wing without ice as a reference, or such as the sequence of images that provide a cue on how the image is changing, the physical features can be better interpreted from the intensity texture map. Here, an image processing scheme similar to the human visual system is applied, where the images are analyzed in the context of the whole video sequence to identify features in the ice formations. The total image change I_{ref}^i and the image time derivative ΔI^i are used to extract information about the transient icing processes. Figure 6 illustrates how these quantities are derived from the image data. The initial
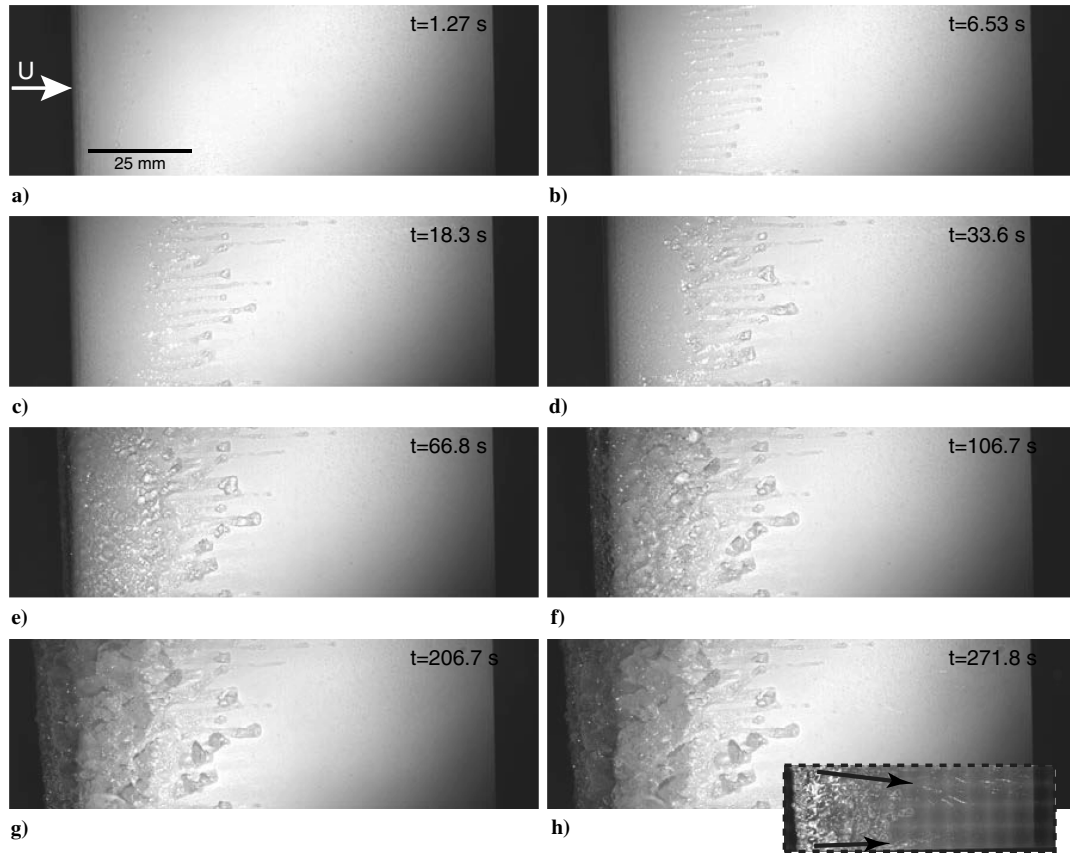
Fig. 3   Snapshots of ice accretion process on the airfoil with the freestream velocity, $U = 40$ m/s; $\alpha = 5$ deg; LWC $= 1.1$ g/m^3; and $T = -8°$C.
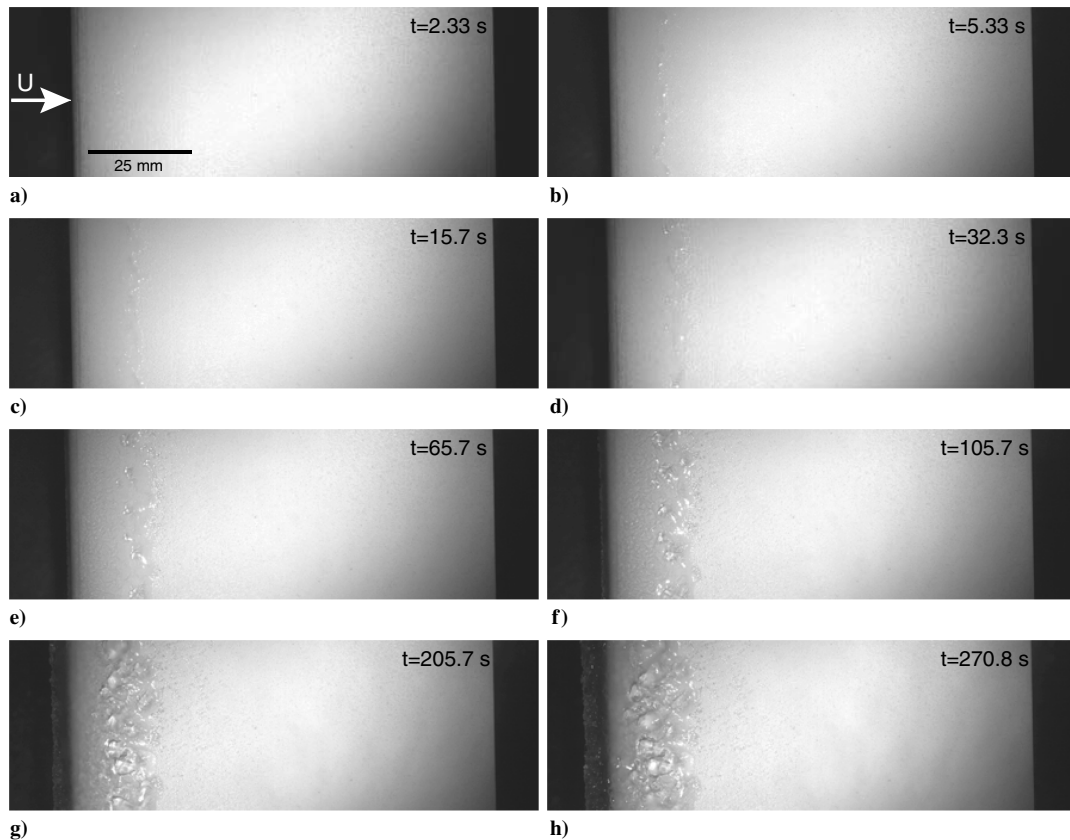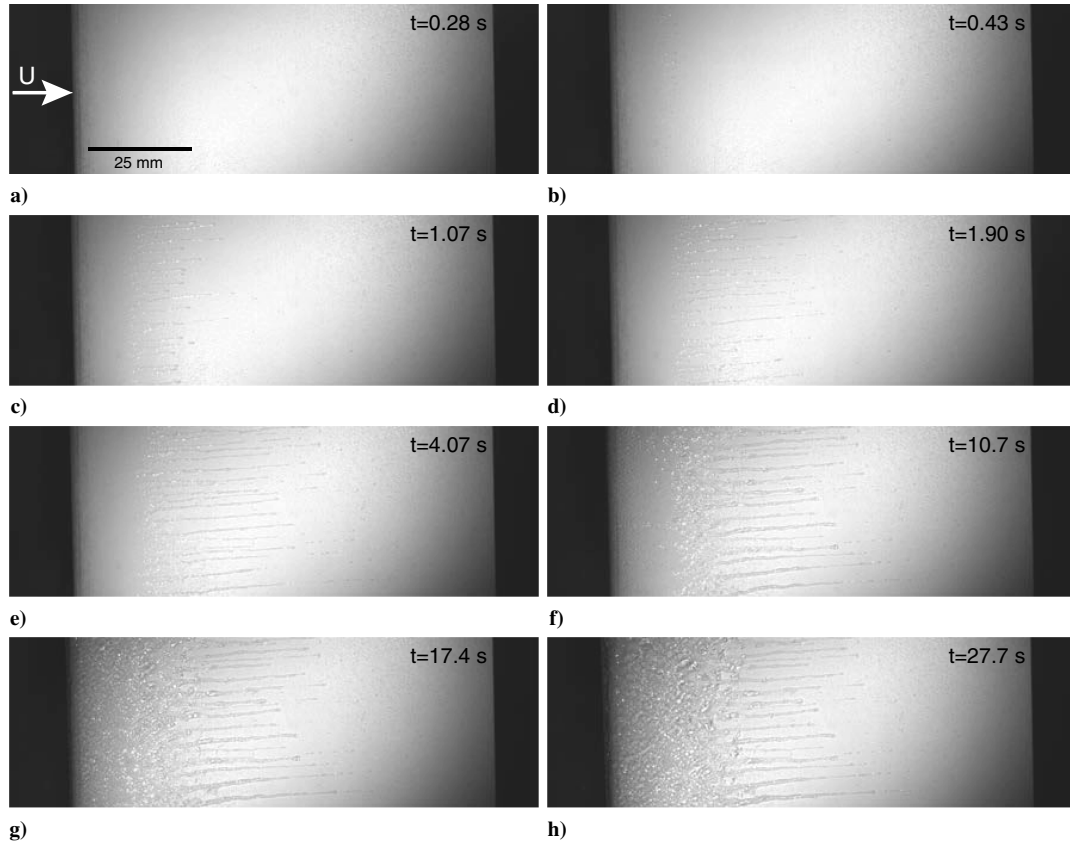

Fig. 4   Snapshots of ice accretion process on the airfoil with the freestream velocity, $U = 20$ m/s; $\alpha = 5$ deg; LWC $= 1.1$ g/m^3; and $T = -8$ °C.

Fig. 5   Snapshots of ice accretion process on the airfoil with the freestream velocity, $U = 60$ m/s; $\alpha = 5$ deg; LWC $= 1.1$ g/m^3; and $T = -8°$C.

reference image of the wing without water or ice is shown in Fig. 6a, and two snapshots of the wing during the icing process separated by a short time interval are shown in Figs. 6b and 6c. Figures 6d and 6e show the intensity difference maps from using the initial wing reference image [Eq. (5)] and from using the previous time image as a reference [Eq. (6)], respectively. Mathematically, these images are expressed as

$$I_{\text{ref}}^i = I^i - I^0 \tag{5}$$
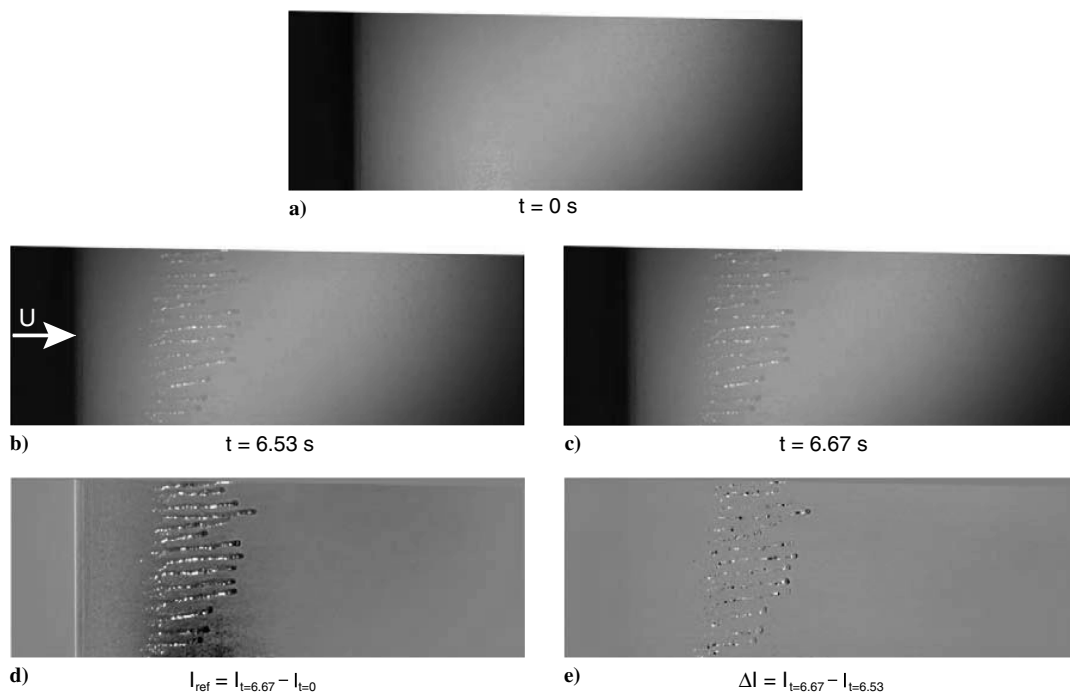
$$\Delta I^i = I^i - I^{i-1} \tag{6}$$

Fig. 6   Source and processed images for ice feature extraction: a) reference image; b, c) icing images; d) differences from reference image (contrast enhanced); e) difference between successive images (contrast enhanced).
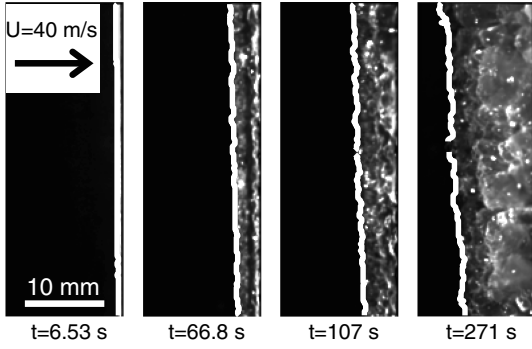
Fig. 7 Leading-edge ice time sequence.

A. Leading-Edge Ice Measurement

Differencing the images with the initial reference produces an intensity map where the pixel counts represent the amount that the image has changed from the initial state. Physically, the difference in intensity must be caused by the presence of water or ice (neglecting image noise). Figure 7 shows the leading-edge ice growth as a function of time. The data were calculated by identifying the first location in front of the wing with meaningful change in the pixel count compared to the initial reference; namely, for every span position y,

$$x^i_{LE} = \text{first}(I^i_{ref}(x)^2 > \epsilon) \tag{7}$$

The value of ϵ should be determined by the intrinsic noise (e.g., sensor noise, light flicker, etc.) in the acquired images. To make false ice detection statistically unlikely, ϵ was chosen as the maximum of four standard deviations of the typical image noise versus four pixel counts (i.e., 2 bits). The imaging noise was characterized by calculating the rms pixel fluctuations between two successive images before the beginning of icing. Typically, one noise standard deviation was about 0.25 pixel counts; therefore, in practice, $\epsilon = 4$.

The resulting time series of leading-edge profiles is further reduced to the average leading-edge thickness, and the rms fluctuation about the straight line fit through the extracted profile. Therefore, the measurement characterizes evolution of the leading-edge ice thickness and the leading-edge roughness.

B. Rivulet Geometry Measurement

Unlike the leading-edge ice that develops over an unlit background, the rivulets form over the wing, which results in relatively low contrast total image differences I_{ref} because both the bare and rivulet-covered wing surfaces scatter light with similar intensity. However, as the rivulets advance along the wing, their convex geometry results in an optical lens effect, which results in large differences between successive images as the rivulet advances. Here, a dark rivulet outline occurs because of the rivulet curvature, whereas bright regions occur at the center of the leading rivulet drop where light is collected, and specular reflections occur at the edge of the rivulet where the surface normal reflects the illumination toward the camera, producing saturated pixel regions. Differencing sequential images produces an intensity map where the pixel counts highlight the regions that are changing due to the presence of water and/or ice. Whether the image intensity differences are positive or negative is not important; however, a large absolute value of the image change indicates significant changes in the water or ice. Because the rivulet geometry is traced out during the runback process, integrating the square of the image derivatives results in an intensity map that highlights the projection of the rivulet geometry onto the surface of the wing.

Figure 8 outlines the process for digitizing the rivulets. First, the rivulet image $\mathcal{A}$ (Fig. 8a) is computed according to Eq. (8), where the median filter rejects any flood illumination flicker noise, squaring the image emphasizes large positive and negative changes in intensity due to rivulet motion, and integrating in time highlights the entire path traced by the rivulet during formation. Next, the image region containing the rivulets is identified and cropped (Fig. 8b). Thresholding allows the image to be partitioned into rivulet and nonrivulet regions, where nonrivulet pixels are zeroed. Finally, the rivulet image is summed along the chord direction, reducing the data to a rivulet image distribution across the span (Fig. 8c):

$$\Delta I^i_f(x, y) = \Delta I^i(x, y) - \text{Median Filter}(\Delta I^i(x, y))$$
$$\mathcal{A}(x, y) = \Sigma_i \Delta I^i_f(x, y)^2 \tag{8}$$

C. Runback Time Series

To track the transient runback, the time sequence of the image time derivatives was used to locate the regions on the wing where water and ice activity causes fluctuations in the recorded images. The spanwise-averaged icing activity A was calculated according to Eq. (9); therefore, each time and chordwise position is mapped to a value describing how much the image was changing across the span due to icing (Fig. 9). By digitizing the contour map of this image/icing activity A, the time evolution of various features during the icing process (e.g., the water film and rivulet runback) was extracted. Figure 9 shows the digitized map of the icing activity and compares a snapshot from the recorded video with the corresponding digitized
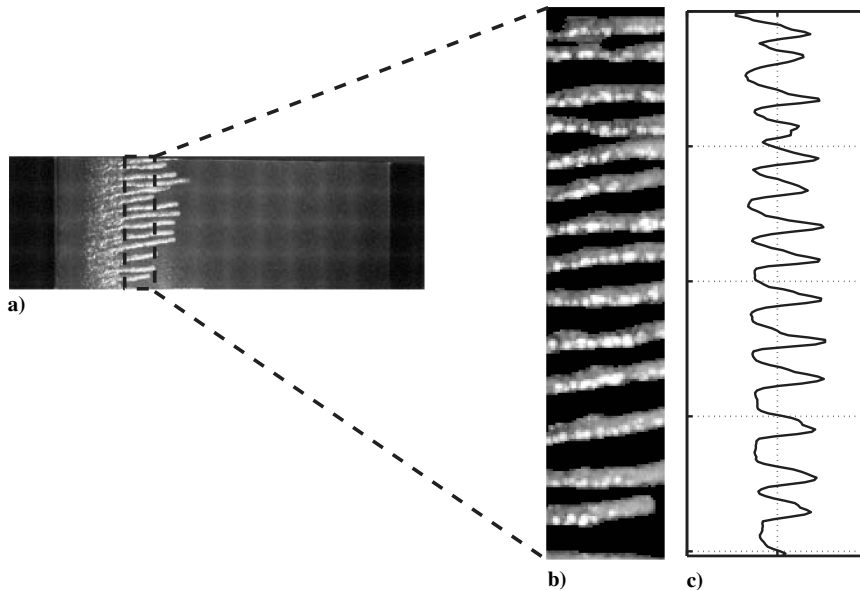

Fig. 8 Rivulet digitization process: a) rivulet image; b) rivulet region; and c) chordwise sum of rivulet region image.
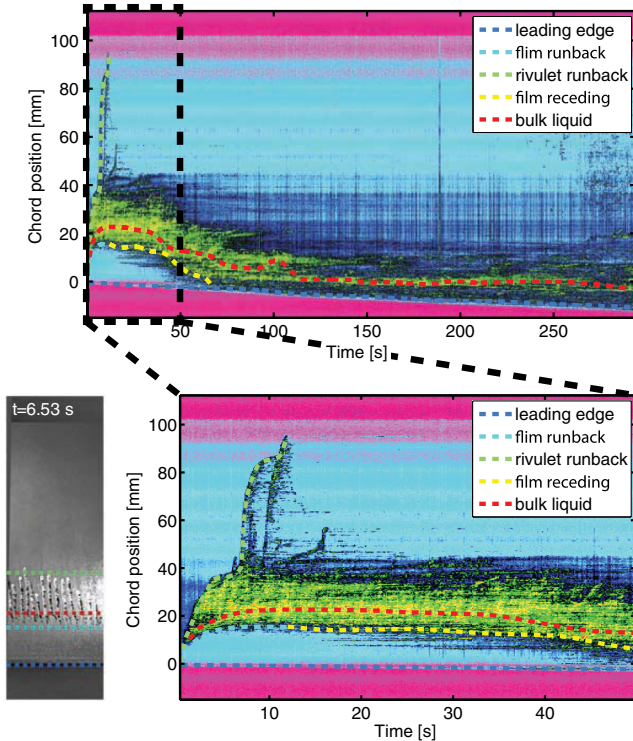
Fig. 9 Overview of image activity A (top) and a zoomed view during initial runback with a snapshot indicating tracked features (bottom). The plots show $\log(A)$ to highlight low-level details.

Fig. 10 Development of the leading-edge ice thickness ($U = 20$ and 40 m/s). Solid lines use Sec. IV.A method, and dotted lines indicate roughness size. Dashed lines use Sec. IV.C method.

features indicated. Icing feature time sequences were digitized by manually clicking the features in the activity map and assigning them labels according to the physical process they represent. The manually clicked points were interpolated using a shape-preserving cubic interpolant to provide a feature location estimate at all times throughout the duration of the icing event:

$$\Delta I_f^i(x, y) = \Delta I^i(x, y) - \text{Median Filter}(\Delta I^i(x, y)) \qquad (9)$$

$$A^i(x) = \Sigma_y \Delta I_f^i(x, y)^2 \qquad (10)$$

First, the leading-edge ice growth was digitized using this activity map method and compared to the previous measurement outlined in Sec. IV.A to provide a comparison and validation of this method for digitizing the runback features. The leading-edge ice thickness is shown in Fig. 10 using coarse dashed lines. The good agreement between the two measurements is evidence that digitizing the activity map provides an accurate measure of the time-evolution of the transient icing features.

Five different icing features are digitized in Fig. 9: the leading-edge ice thickness, the location of the water film front during the initial runback, the location of the maximum rivulet runback, the location of the receding water film, and the location of maximum image activity (denoted "bulk liquid"). In the case of the leading-edge ice thickness, the film runback, and the film recession, the features were identified as the first chordwise location where the image activity map deviated significantly from the background levels. Conversely, the rivulet runback feature was identified as the rearmost chordwise location image activity map deviated significantly from the background levels. The maximum image activity location was identified approximately along the ridge corresponding to the maximum image activity and represents the region where the water interacts with growing ice roughness features, leading to pooling and rapidly changing images due to ice growth and water surface waves.
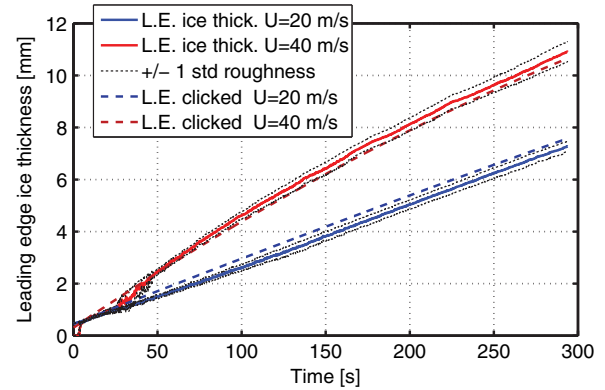
V. Results and Discussion

A. Leading-Edge Ice

The topdown two-dimensionally projected view provides a measurement of the ice accretion dimensions that lie within the measurement plane; thus, the measurement captures the thickness of the ice that forms on the leading edge, and it captures the lateral extents of the features on the wing. Measuring the dimensions in the chord-span binormal direction requires a different technique, such as the digital image projection [20].

Figure 10 shows the long-time growth of the leading-edge ice for $U = 20$ and 40 m/s trials. The accumulated ice is proportional to the accumulation parameter a given in Eq. (4). Here, the time derivative of the accumulation parameter relates to the rate of ice accumulation; namely,

$$\frac{\mathrm{d}a}{\mathrm{d}\tau} = \frac{\text{LWC} \cdot U}{L} \qquad (11)$$

The rate of accumulation is proportional to the freestream velocity, which is reflected in the measured leading-edge ice thickness growth as the freestream velocity is approximately doubled from $U = 20$ to 40 m/s (Fig. 10). In less than 5 min, the leading-edge ice growth exceeds 7 and 10 mm at $U = 20$ and 40 m/s, respectively. Compared to the maximum wing thickness of 12.2 mm, this represents a significant change in the airfoil shape.

Additionally, the dotted lines in Fig. 10 indicate the ± 1 standard deviation of the roughness variations about the mean location. As the leading-edge ice develops and grows, so does the roughness of the ice features at the leading edge. Previous work has shown that the stagnation point at the leading edge of an airfoil in glaze ice conditions is unstable and develops three-dimensional disturbances at low Mach numbers [22]. These disturbances grow and manifest themselves as ice roughness at the leading edge.

B. Rivulet Geometry

The formation of rivulets during the initial runback is a process that plays an important role in the formation of ice downstream of the leading-edge ice growth. As the ice at the leading edge grows, it acts as a barrier to the collection of water on the wing surfaces behind it, especially if the flow separates over the leading-edge ice growth; however, the rivulets may still stick out into the separated flow, where it can continue to collect water and continue to grow. This process is a positive feedback loop where ice features that protrude out the farthest grow the fastest [10]. Additionally, the rivulets themselves can lead to detrimental aerodynamic performance by increasing turbulence, leading to decreased lift-to-drag ratios [23]. The geometry of the rivulets is important to determining the aerodynamic effect, with larger rivulets resulting in decreased aerodynamic performance.
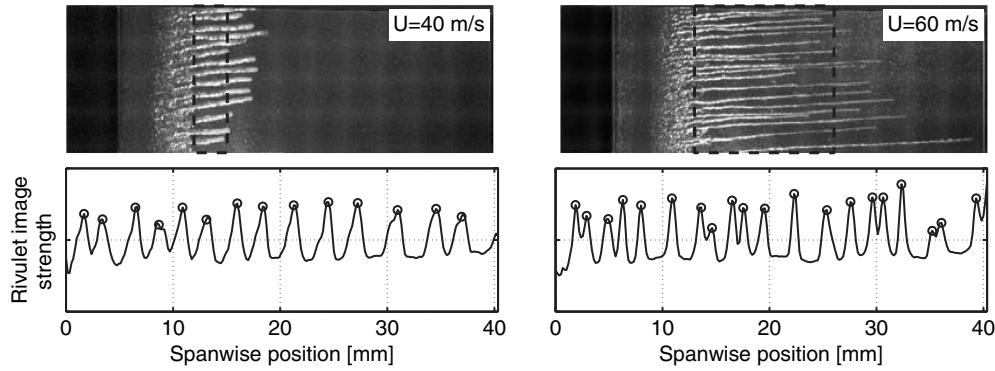
Fig. 11   Digitized rivulet structure: rivulet images with boxes around analysis regions (top) and rivulet intensity profiles with circles at extracted locations (bottom).

The measured rivulet geometry is shown in Fig. 11, with the processed image data on top highlighting the configuration of the rivulets on the wing and with the digitized rivulet locations shown below. For each case, the rivulet geometry was calculated using the regions within the dashed-line box. The extracted rivulet geometries are summarized in Table 1. Here, the number of rivulets, N, is given for the span field of view as pictured in Fig. 8; the spacing δ is the mean center-to-center spacing between neighboring rivulets; the area fraction AF is the area covered by the rivulets versus the total area in the rivulet region, namely the fraction of Fig. 8b with nonzero pixel data; and the rivulet width w is the mean width across a single rivulet. As illustrated in Sec. III, the slowest-wind-speed case produced no rivulets. This is an important difference between icing conditions and conditions with water present but without freezing temperatures. Pervious water runback measurements show that rivulet formation does occur at lower wind speeds [20] in the absence of freezing conditions, which demonstrates that the rivulet width decreases with increasing wind speed. Here, the measured rivulets spacing and width decrease with increased freestream velocity. Furthermore, the rivulet width decreases faster than the rivulet spacing such that rivulet area fraction (the rivulet area divided by the total area covered by rivulets) decreases with increasing wind speed.

C.   Icing Runback

The ice accretion process on the wing begins with runback of the water film and its breakup into rivulets. This process transports water from the collection area to other regions of the wing, playing an important role in the final ice shape. The runback is driven by the aerodynamic shear stress. Figure 12 compares the measured film and rivulet runback for the three wind speeds tested. The film runback location measures the extent of the very thin water film. In contrast, the rivulets form as the aerodynamic shear stress drives a flow toward the contact line, where water accumulates and the water thickness increases [24]. Eventually the advancing film front breaks into rivulets and runs back. In the case of $U = 20$ m/s, where no rivulets formed, the maximum film runback region is shown, which consists of the thicker water beading up at the contact line, which is similar to the water beads advancing at the head of the rivulets.

With increasing wind speed, high shear stress drives the film and rivulet flows. Figure 12 shows that the film and rivulets advance more quickly at higher speed. The fastest wind speed tested had rivulet runback speeds reaching $u_{\rm riv} = 53.8$ mm/s. The mean film and rivulet runback speeds are summarized in Table 2. Here, the mean speed is calculated from the data in Fig. 12 by dividing the total
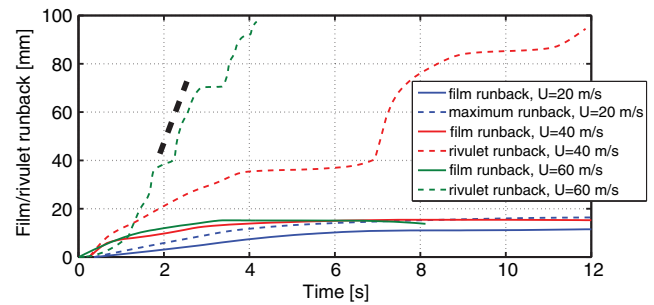

Fig. 12   Time evolution of the film and rivulet runback. Maximum runback speed $u_{\rm riv} = 53.8$ mm/s at $U = 60$ m/s as denoted by the heavy dashed line.

runback distance by the time until the maximum runback distance was reached; in cases such as the $U = 40$ m/s rivulet runback, the instantaneous velocity may sometimes be much higher. Surprisingly, the film advances farther along the chord at higher wind speeds as well. This is in contrast to simple water runback experiments without freezing conditions [20], where film extent decreased with increasing wind speed, instead forming rivulets farther upstream. This difference between freezing and nonfreezing conditions indicates that the heat transfer process that governs the rate of ice formation also plays an important role in the formation of the rivulets.

The stair-step shape of the rivulet runback extent in the $U = 40$ and 60 m/s measurements (Fig. 12) demonstrates that the rivulet runback is not a continuous process. Here, the rivulet runs back for a short distance and then becomes pinned before running back again. The rivulet may freeze or simply become too diminished in volume to further advance the contact line. The runback continues when enough upstream water beads up and travels along the rivulet until it meets the rivulet head and continues the rivulet advancement. This process is illustrated in the bottom icing activity map in Fig. 9 along the broken line denoting the "rivulet runback" feature. Initially, the rivulet runs

Table 2   Measured mean water film and rivulet runback speed

Freestream U, m/s	Film runback $u_{\rm film}$, mm/s	Rivulet runback $u_{\rm riv}$, mm/s
20	1.23	2.38
40	3.14	7.96
60	4.66	23.3

Table 1   Extracted rivulet geometry

Freestream U, m/s	Number of rivulets N	Spacing δ, mm	Area fraction AF	Width w, mm
20	0	— —	— —	— —
40	14	2.71 ± 0.60	0.50	1.35
60	17	2.09 ± 0.93	0.29	0.65

back beyond the 80 mm chord position before stalling at the time around $t = 10.0$ s. A second bead of water begins to propagate along the rivulet path starting around $t = 10.5$ s until it catches up to the end of the rivulet at $t = 11.0$ s, where it advances the rivulet another 10 mm.

VI. Conclusions

This work has presented results of wind-tunnel icing experiments on a NACA 0012 wing. High-speed video shows the transient process involved in determining the ice shapes on the wing. Image processing techniques were implemented to make quantitative measurements of key icing features involved in the transient icing processes. The tools developed here provide a method for investigating the transient icing physics, which have been largely been ignored in previous wind-tunnel icing studies.

The measurements make use of the time-resolved image sequences of the icing process to extract features based on image differences from a reference image as well as from sequential image differences. The long-term ice accretion at the leading edge was found to grow according to the accumulation rate of water. The agreement between the two different measurement techniques for extracting leading-edge ice thickness validate the icing activity map method for extracting the time-evolution of transient icing features on the wing, allowing the water film and rivulet runback processes to be quantified.

Acknowledgments

References

[1] Politovich, M. K., "Predicting Glaze or Rime Ice Growth on Airfoils," *Journal of Aircraft*, Vol. 37, No. 1, Jan. 2000, pp. 117–121.
doi:10.2514/2.2570
[2] Rothmayer, A. P., "Scaling Laws for Water and Ice Layer on Airfoils," *41st Aerospace Sciences Meeting and Exhibit*, AIAA Paper 2003-1217, Jan. 2003.
doi:10.2514/6.2003-1217
[3] Al-Khalil, K. M., Keith, T. G., and DeWitt, K. J., "Development of an Anti-Icing Runback Model," *28th Aerospace Sciences Meeting*, AIAA Paper 1990-0759, Jan. 1990.
doi:10.2514/6.1990-759
[4] Ueno, K., and Farzaneh, M., "Linear Stability Analysis of Ice Growth Under Supercooled Water Film Driven by a Laminar Airflow," *Physics of Fluids*, Vol. 23, No. 4, April 2011, Paper 042103.
doi:10.1063/1.3575605
[5] Fortin, G., Laforte, J.-L., and Ilinca, A., "Heat and Mass Transfer During Ice Accretion on Aircraft Wings with an Improved Roughness Model," *International Journal of Thermal Sciences*, Vol. 45, No. 6, June 2006, pp. 595–606.
doi:10.1016/j.ijthermalsci.2005.07.006
[6] Gent, R. W., Dart, N. P., and Cansdale, J. T., "Aircraft Icing," *Philosophical Transactions of the Royal Society of London A*, Vol. 358,

No. 1776, Nov. 2000, pp. 2873–2911.
doi:10.1098/rsta.2000.0689
[7] Tsao, J. C., and Rothmayer, A. P., "Application of Triple-Deck Theory to the Prediction of Glaze Ice Roughness Formation on an Airfoil Leading Edge," *Computers and Fluids*, Vol. 31, No. 8, Nov. 2002, pp. 977–1014.
doi:10.1016/S0045-7930(01)00050-0
[8] Henry, R. C., Hansman, R. J., and Breuer, K. S., "Heat Transfer Variation on Protuberances and Surface Roughness Elements," *Journal of Thermophysics and Heat Transfer*, Vol. 9, No. 1, Jan. 1995, pp. 175–180.
doi:10.2514/3.644
[9] Bragg, M., Broeren, A., and Blumenthal, L., "Iced-Airfoil Aerodynamics," *Progress in Aerospace Sciences*, Vol. 41, No. 5, July 2005, pp. 323–362.
doi:10.1016/j.paerosci.2005.07.001
[10] Olsen, W., and Walker, E., "Experimental Evidence for Modifying the Current Physical Model for Ice Accretion on Aircraft Surfaces," NASA TM-87184, May 1986.
[11] Homola, M. C., Nicklasson, P. J., and Sundsbø, P. A., "Ice Sensors for Wind Turbines," *Cold Regions Science and Technology*, Vol. 46, No. 2, Nov. 2006, pp. 125–131.
doi:10.1016/j.coldregions.2006.06.005
[12] Shin, J., and Bond, T. H., "Repeatability of Ice Shapes in the NASA Lewis Icing Research," *Journal of Aircraft*, Vol. 31, No. 5, Sept. 1994, pp. 1057–1063.
doi:10.2514/3.46610
[13] Addy, H. E., "Ice Accretions and Icing for Modern Airfoils Effects," NASA TP-2000-210031, April 2000.
[14] Anderson, D. N., "Acceptable Tolerances for Matching Icing Similarity Parameters in Scaling Applications," *39th Aerospace Sciences Meeting and Exhibit*, AIAA Paper 2001-0832, Jan. 2001.
doi:10.2514/6.2001-832
[15] Vargas, M., and Tsao, J. C., "Observations on the Growth of Roughness Elements into Icing Feathers," *45th AIAA Aerospace Sciences Meeting and Exhibit*, AIAA Paper 2007-0900, Jan. 2007.
doi:10.2514/6.2007-900
[16] Vargas, M., and Reshotko, E., "LWC and Temperature Effects on Ice Accretion Formation on Swept Wings at Glaze Ice Conditions," NASA TM-2000-209777, Jan. 2000.
[17] Vargas, M., Broughton, H., Sims, J. J., Bleeze, B., and Gaines, V., "Local and Total Density Measurements in Ice Shapes," NASA TM-2005-213440, March 2005.
doi:10.2514/1.23326
[18] Tsao, J. C., and Lee, S., "Evaluation of Icing Scaling on Swept NACA 0012 Airfoil Models," NASA CR-2012-217419, June 2012.
[19] Kraj, A. G., and Bibeau, E. L., "Phases of Icing on Wind Turbine Blades Characterized by Ice Accumulation," *Renewable Energy*, Vol. 35, No. 5, May 2010, pp. 966–972.
doi:10.1016/j.renene.2009.09.013
[20] Zhang, K., Johnson, B., Rothmayer, A., and Hu, H., "An Experimental Investigation on Wind-Driven Rivulet/Film Flows over a NACA0012 Airfoil by Using Digital Image Projection Technique," *52nd Aerospace Sciences Meeting*, AIAA Paper 2014-0741, Jan. 2014.
doi:10.2514/6.2014-0741
[21] Hartley, D., and Murgatroyd, W., "Criteria for the Break-Up of Thin Liquid Layers Flowing Isothermally over Solid Surfaces," *International Journal of Heat and Mass Transfer*, Vol. 7, No. 9, 1964, pp. 1003–1015.
doi:10.1016/0017-9310(64)90042-0
[22] Otta, S., and Rothmayer, A., "Instability of Stagnation Line Icing," *Computers and Fluids*, Vol. 38, No. 2, 2009, pp. 273–283.
doi:10.1016/j.compfluid.2008.02.005
[23] Thompson, B. E., and Jang, J., "Aerodynamic Efficiency of Wings in Rain," *Journal of Aircraft*, Vol. 33, No. 6, Nov. 1996, pp. 1047–1053.
doi:10.2514/3.47056
[24] Eres, M. H., Schwartz, L. W., and Roy, R. V., "Fingering Phenomena for Driven Coating Films," *Physics of Fluids*, Vol. 12, No. 6, June 2000, pp. 1278–1295.
doi:10.1063/1.870382